

Diffusion-Based Impedance Learning for Contact-Rich Manipulation Tasks

Noah Geiger, Tamim Asfour, Neville Hogan and Johannes Lachner

Abstract—Learning methods excel at motion generation in the information domain but are not primarily designed for physical interaction in the energy domain. Impedance Control shapes physical interaction but requires task-aware tuning by selecting feasible impedance parameters. We present Diffusion-Based Impedance Learning, a framework that combines both domains. A Transformer-based Diffusion Model with cross-attention to external wrenches reconstructs a simulated Zero-Force Trajectory (sZFT). This captures both translational and rotational task-space behavior. For rotations, we introduce a novel SLERP-based quaternion noise scheduler that ensures geometric consistency. The reconstructed sZFT is then passed to an energy-based estimator that updates stiffness and damping parameters. A directional rule is applied that reduces impedance along non-task axes while preserving rigidity along task directions. Training data were collected for a parkour scenario and robotic-assisted therapy tasks using teleoperation with Apple Vision Pro. With only tens of thousands of samples, the model achieved sub-millimeter positional accuracy and sub-degree rotational accuracy. Its compact model size enabled real-time torque control and autonomous stiffness adaptation on a KUKA LBR iiwa robot. The controller achieved smooth parkour traversal within force and velocity limits and 30/30 success rates for cylindrical, square, and star peg insertions without any peg-specific demonstrations in the training data set. All code for the Transformer-based Diffusion Model, the robot controller, and the Apple Vision Pro telemanipulation framework is publicly available. These results mark an important step towards Physical AI, fusing model-based control for physical interaction with learning-based methods for trajectory generation.

Index Terms—Imitation learning, Diffusion Models, Physical interaction, Impedance Control

I. INTRODUCTION

Robotic behavior emerges at the interface of two fundamentally different domains. Motion planning belongs to the *information domain*, where learning-based methods have recently shown remarkable progress. In contrast, physical interaction is governed by the *energy domain*, and model-based Impedance Control has been widely adopted to guarantee stability [1] and safety [2]. Robots that manipulate in unstructured environments must bridge these domains: motions must be inferred as information, yet executed through stable, energy-consistent

N. Geiger and T. Asfour are with the Institute for Anthropomatics and Robotics, Karlsruhe Institute of Technology, Karlsruhe, Germany; e-mail: noah.geiger@student.kit.edu, asfour@kit.edu

N. Geiger, N. Hogan, and J. Lachner are with the Department of Mechanical Engineering, Massachusetts Institute of Technology, Cambridge, USA; N. Hogan, and J. Lachner are also with the and Department of Brain and Cognitive Sciences, Massachusetts Institute of Technology, Cambridge, USA; e-mail: ngeiger@mit.edu, neville@mit.edu, jlachner@mit.edu

This work has been submitted to the IEEE for possible publication. Copyright may be transferred without notice, after which this version may no longer be accessible.

exchange with the environment [3]. This requirement is critical in assembly, rehabilitation, and other contact-rich tasks where visual feedback is limited and success depends on regulating interaction rather than simply following a path.

While Impedance Control provides the framework for shaping robot–environment interaction [4], its performance critically depends on selecting appropriate stiffness and damping parameters (which may need to be adapted online) [5]. Too much stiffness can lead to jamming, too little can prevent task execution.

Recent advances in contact-rich manipulation can be divided into two main strands. *Model-based approaches* incorporate explicit contact dynamics like friction cones, complementarity constraints, and mixed-integer formulations [6]–[14]. These methods produce behavior consistent with physical contact but face challenges: high computational cost, parameter sensitivity, and limited robustness in unstructured settings. *Learning-based approaches*, in contrast, operate in the information domain. Reinforcement learning and sampling-based optimization [15]–[18], along with more recent generative models such as diffusion policies [19], flow-matching policies [20], [21], and Transformer-based policy models [22], [23], excel at motion generation across tasks and embodiments [24]. However, execution in these frameworks often relies on velocity-based or fixed-gain PD controllers. While fixed-gain PD controllers can avoid hardware damage, apparent compliance is only a byproduct of low control gains. In unstructured environments, where vision may be unreliable or occluded, explicit impedance regulation is essential to control interaction.

The Adaptive Compliance Policy of [25] is a first step toward combining generative models with compliance adaptation, but it is formulated within an admittance-control framework. Admittance control is known to struggle with transitions into and out of contact [4], [26], making it unsuitable for many assembly tasks such as peg-in-hole insertion. To our knowledge, no approach has successfully combined learning-based trajectory generation (information domain) with impedance adaptation (energy domain).

This paper addresses that gap. We present *Diffusion-Based Impedance Learning*, a framework that unifies generative modeling with energy-consistent Impedance Control. A conditional Transformer-based Diffusion Model reconstructs simulated Zero-Force Trajectories¹ from contact-perturbed displacement and external wrench signals. The sZFT serves as a reconstructed equilibrium used to modulate task-space impedance.

¹The Zero-Force Trajectory (ZFT), introduced by Hogan [5], refers to the commanded equilibrium motion in the unconstrained case: the unique end-effector pose at which the interaction wrench vanishes.

A directional adaptation scheme adapts stiffness primarily along non-task-relevant directions and preserves rigidity where needed for execution. In this way, our approach combines the strengths of learning-based methods (motion generation in the information domain) with those of model-based methods (impedance regulation in the energy domain).

We validate the framework on a KUKA LBR iiwa in two contact-rich scenarios: parkour-style obstacle traversal and multi-geometry peg-in-hole insertion. Training data were collected through telemanipulation, using Apple Vision Pro (AVP) equipped with a markerless pose tracking framework [27] integrated into the robot controller. Both tasks highlight the shortcomings of fixed impedance and simple adaptation schemes, which either jam at obstacles or fail to achieve insertion. In contrast, Diffusion-Based Impedance Learning achieves consistent success. The outcomes of Table I preview the central result of this work: bridging the information and energy domains is key to robust manipulation in unstructured environments.

All code for the Transformer-based Diffusion Model, the robot controller, and the Apple Vision Pro telemanipulation framework is available on our GitHub repository². Demonstration videos of all experiments can be found on the project website³.

II. METHODS

We outline the process in both domains: Transformer-based diffusion in the information domain and energy-based Impedance Control in the energy domain. These components are then fused through diffusion-based reconstruction of simulated Zero-Force Trajectories (sZFT).

A. Diffusion Models

Diffusion Models learn to sample from a data distribution by approximating the reverse-time dynamics of a Gaussian diffusion process. Let $\{z_i\}_{i=1}^N$ be independent and identically distributed samples from the data distribution p_{data} ; we posit a parametric family of distributions $\{p_\theta\}_{\theta \in \Theta}$ and learn θ so that $p_\theta \approx p_{\text{data}}$. A forward Markov chain maps a clean sample z_0 to (approximately) $\mathcal{N}(0, \mathbf{I})$ over T steps. The learned reverse-time chain iteratively denoises z_t to produce a sample that approximates p_{data} (Figure 1).

1) *Forward Diffusion*: The forward diffusion process defines a Markov chain with Gaussian transitions

$$q(z_t | z_{t-1}) = \mathcal{N}(\sqrt{\alpha_t} z_{t-1}, (1 - \alpha_t) \mathbf{I}), \quad (1)$$

where $\alpha_t := 1 - \beta_t$ and $\{\beta_t\}_{t=1}^T \subset (0, 1)$ is a predefined noise schedule. The quantity $(1 - \alpha_t) = \beta_t$ is the per-step diffusion variance, which controls the signal-to-noise ratio across time. After T steps with $\bar{\alpha}_T := \prod_{i=1}^T \alpha_i \approx 0$, the marginal distribution approaches a standard normal distribution, $z_T \approx \mathcal{N}(0, \mathbf{I})$. The marginal distribution at step t has the closed form

$$q(z_t | z_0) = \mathcal{N}(\sqrt{\bar{\alpha}_t} z_0, (1 - \bar{\alpha}_t) \mathbf{I}), \quad (2)$$

which admits the equivalent reparameterization

$$z_t = \sqrt{\bar{\alpha}_t} z_0 + \sqrt{1 - \bar{\alpha}_t} \varepsilon, \quad \varepsilon \sim \mathcal{N}(0, \mathbf{I}). \quad (3)$$

²<https://github.com/StrokeAIRObotics/DiffusionBasedImpedanceLearning>

³<https://strokeairobotics.github.io/DiffusionBasedImpedanceLearning>

2) *Noise schedule*: The per-step variances $\{\beta_t\}_{t=1}^T$ define the noise schedule, which controls how the signal-to-noise ratio $\text{SNR}_t = \bar{\alpha}_t / (1 - \bar{\alpha}_t)$ decays from ∞ to 0 over time. A well-chosen schedule balances the complexity of denoising, keeping early steps near-deterministic and later steps close to pure noise. [29], [30]

3) *Reverse Process and Learning Objective*: The true reverse $q(z_{t-1} | z_t)$ is intractable, as it marginalizes over z_0 . However, since the forward chain is linear-Gaussian, the posterior $q(z_{t-1} | z_t, z_0)$ is itself Gaussian with mean $\tilde{\mu}_t(z_t, z_0)$ and variance $\tilde{\beta}_t \mathbf{I}$ [31]. We model $p_\theta(z_{t-1} | z_t) = \mathcal{N}(\mu_\theta(z_t, t), \Sigma_\theta(z_t, t))$ and fit θ by minimizing the variational bound $\sum_t D_{\text{KL}}(q(z_{t-1} | z_t, z_0) \| p_\theta(z_{t-1} | z_t))$. With the ε -parameterization,

$$\mu_\theta(z_t, t) = \frac{1}{\sqrt{\alpha_t}} \left(z_t - \frac{\beta_t}{\sqrt{1 - \bar{\alpha}_t}} \varepsilon_\theta(z_t, t) \right),$$

and $z_t = \sqrt{\bar{\alpha}_t} z_0 + \sqrt{1 - \bar{\alpha}_t} \varepsilon$, the objective reduces (up to constants) to the noise-prediction loss [30]:

$$\mathcal{L}_{\text{simple}}(\theta) = \mathbb{E}_{t, z_0, \varepsilon} \left[\|\varepsilon - \varepsilon_\theta(\sqrt{\bar{\alpha}_t} z_0 + \sqrt{1 - \bar{\alpha}_t} \varepsilon, t)\|_2^2 \right].$$

4) *Training and Inference Algorithms*: Training follows a noise-prediction objective: at each iteration a clean sample $z_0 \sim p_{\text{data}}$, a timestep $t \in \{1, \dots, T\}$ (uniform), and Gaussian noise $\varepsilon \sim \mathcal{N}(0, \mathbf{I})$ are sampled. The closed-form forward diffusion produces z_t and the network ε_θ is updated to minimize mean-squared error between ε and its prediction $\varepsilon_\theta(z_t, t)$ [30], [32]. At inference, generation starts from $z_T \sim \mathcal{N}(0, \mathbf{I})$ and applies the learned reverse transitions $p_\theta(z_{t-1} | z_t)$ for $t=T, \dots, 1$, yielding z_0 as a sample from the model [30]. For robotic trajectory generation, this iterative denoising maps pure noise into trajectories that are consistent with task goals (Figure 1).

5) *Conditional Diffusion*: To generate task-consistent behavior, the denoising process is conditioned on an additional context variable c (e.g., goals, scene state, or interaction wrench). The reverse model and noise predictor then become $p_\theta(z_{t-1} | z_t, c)$ and $\varepsilon_\theta(z_t, t, c)$.

Conditioning can be implemented in several ways, including (i) early fusion (e.g., feature concatenation), (ii) cross-attention over context tokens for Transformer denoisers, or (iii) lightweight fusion layers [33], [34].

In our approach, conditional diffusion is central. By conditioning on external wrenches, the model reconstructs trajectories that are consistent with physical interaction. This ties the denoising process in the information domain to the regulation of interaction in the energy domain.

More details about Diffusion Models can be found in [30], [32], [35], [36].

6) *Transformer-based Diffusion Model*: In this paper, we choose a Transformer-based denoising network since robotic trajectories are time series and context-dependent effects (e.g., contact events with delayed consequences). Self-attention provides a content-based global receptive field and fully parallelizable training, which is advantageous over Recurrent or Convolutional Neural Networks for sequence modeling [23], [37].

TABLE I: Preview of experimental outcomes (full details in Section IV). Fixed impedance fails in contact-rich tasks, while Diffusion-Based Impedance Learning achieves robust success by reconstructing a contact-consistent sZFT.

Controller	Parkour	Cylindrical Peg	Square Peg	Star Peg
Fixed impedance	✗ (stopped at first obstacle)	30/30	4/30	0/30
Diffusion-Based Impedance Learning	✓ (smooth traversal)	30/30	30/30	30/30

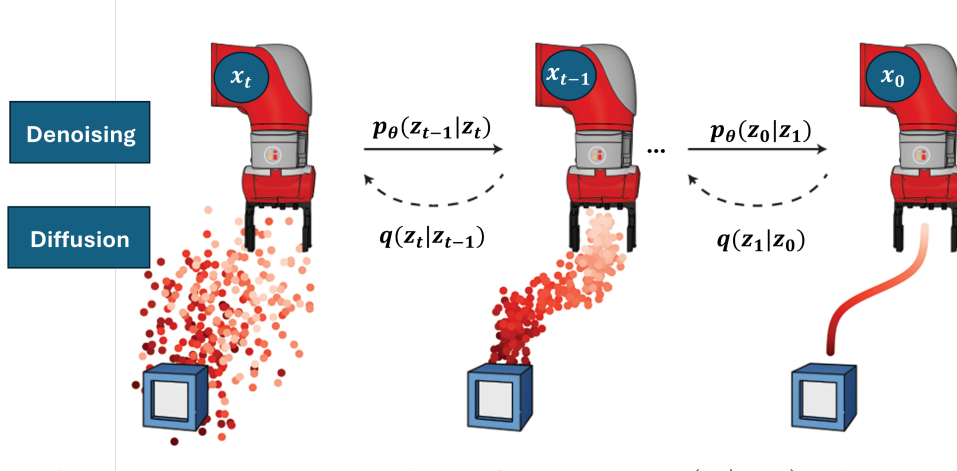


Fig. 1: Diffusion overview. Bottom: dashed arrows depict the forward process $q(z_t | z_{t-1})$ which gradually corrupts a clean trajectory z_0 . Top: solid arrows depict the reverse process $p_{\theta}(z_{t-1} | z_t)$ which is learned to reconstruct structured robotic behavior. Figure adapted from [28].

At each diffusion step, pose tokens are formed from translations and unit-quaternions. These tokens are embedded and enriched with learned positional and timestep embeddings. Interaction signals (forces and moments) are projected to context tokens and integrated through a multi-head cross-attention layer. Here, trajectory tokens serve as queries and context tokens as keys and values. The combined sequence is then processed by stacked self-attention and feed-forward layers, and a lightweight Multi-layer Perceptron head predicts the 7D noise (3D translations and 4D unit-quaternions) for each token. This architecture captures temporal structure while conditioning on interaction signals, a requirement that is central for contact-rich applications [37]–[42].

More details about Transformer-based models can be found in [36], [37], [41], [42].

B. Energy-based Impedance Control

Impedance Control regulates the dynamic relationship between motion and interaction wrenches. Rather than commanding exact positions, the robot behaves like a virtual mechanical system characterized by stiffness, damping, and inertia⁴. In contrast to admittance control⁵, the impedance formulation enables the robot to maintain compliance while ensuring stability when interacting with passive environments [44]–[47].

From an energy perspective, Impedance Control transforms the potential energy stored in a virtual spring to the work done

by external wrenches [48]. Let the pose displacement be

$$\Delta \mathbf{x} = \begin{pmatrix} \mathbf{e}_t \\ \mathbf{e}_r \end{pmatrix} \in \mathfrak{se}(3), \quad (4a)$$

$$\mathbf{e}_t := \mathbf{p} - \mathbf{p}_0 \in \mathbb{R}^3, \quad (4b)$$

$$\mathbf{e}_r := \log(\mathbf{q}_0 \mathbf{q}^{-1}) \in \mathbb{R}^3 \simeq \mathfrak{so}(3). \quad (4c)$$

where the observed pose is $(\mathbf{p}, \mathbf{q}) \in \mathbb{R}^3 \times \mathbb{S}^3$ and the equilibrium pose is $(\mathbf{p}_0, \mathbf{q}_0) \in \mathbb{R}^3 \times \mathbb{S}^3$. Any unit quaternion admits the unit axis-angle representation

$$\mathbf{q} = (\cos(\frac{\theta}{2}), \mathbf{u} \sin(\frac{\theta}{2})), \quad \|\mathbf{u}\| = 1, \quad \theta \in [0, \pi]. \quad (5)$$

In our formulation, the logarithm map is applied to the error quaternion $\mathbf{q}_0 \mathbf{q}^{-1}$ to return the axis-angle error vector $\mathbf{e}_r = \mathbf{u}_0 \theta_0$.

Let $\mathbf{K}_t, \mathbf{K}_r \in \mathbb{R}^{3 \times 3}$ be diagonal, positive semidefinite stiffness matrices and $\mathbf{K} = \text{diag}(\mathbf{K}_t, \mathbf{K}_r)$. Define the potential energy

$$\mathcal{U}(\Delta \mathbf{x}) = \frac{1}{2} \mathbf{e}_t^\top \mathbf{K}_t \mathbf{e}_t + \frac{1}{2} \mathbf{e}_r^\top \mathbf{K}_r \mathbf{e}_r \in \mathbb{R}_{\geq 0}. \quad (6)$$

The spatial wrench $\mathbf{F} = \begin{pmatrix} \mathbf{f} \\ \mathbf{m} \end{pmatrix} \in \mathfrak{se}^*(3)$ can be obtained from the gradient

$$\mathbf{F} = \frac{\partial \mathcal{U}}{\partial \Delta \mathbf{x}}. \quad (7)$$

The damping matrices $\mathbf{B}_t, \mathbf{B}_r \in \mathbb{R}^{3 \times 3}$ are chosen proportional to stiffness,

$$\mathbf{B}_t = \lambda_t \mathbf{K}_t, \quad \mathbf{B}_r = \lambda_r \mathbf{K}_r, \quad (8)$$

⁴And possibly higher-order dynamic effects.

⁵Admittance control requires additional methods to guarantee passivity [43].

with $\lambda_t, \lambda_r > 0$ selected as described in Appendix A-C. This yields Rayleigh-like dissipation that scales with stiffness and task-space inertia.

In addition to this virtual impedance, the environment contributes external wrenches $\mathbf{F}_{\text{ext}} \in \mathfrak{se}^*(3)$. These wrenches arise during both translational motion $\dot{\mathbf{p}} \in \mathbb{R}^3$ and rotational motion $\omega \in \mathfrak{so}(3)$. Finally, the Jacobian $\mathbf{J}(\mathbf{q}) : \mathbb{R}^n \rightarrow \mathfrak{se}(3)$, a function of the joint configuration $\mathbf{q} \in \mathbb{R}^n$, provides the mapping between the n -dimensional joint space and the 6-dimensional task space. An overview of the controller implemented in this paper can be found in Appendix A.

The Impedance Control framework can be illustrated by the Norton equivalent network, as represented in Figure 2. Here, two sources interact through the impedance element:

- The *motion source*, which represents the equilibrium pose $\{\mathbf{p}_0, \mathbf{q}_0\}$ at each point of the ZFT,
- The *impedance source*, which represents the baseline stiffness \mathbf{K} . In our case, damping \mathbf{B} is a function of stiffness and inertia (Appendix A-C).

The environment applies external wrenches \mathbf{F}_{ext} , which are balanced by the virtual spring–damper system. This ensures that the interaction wrenches are consistent both with the energy stored in the virtual spring and with the motion of the robot. This formulation highlights that Impedance Control operates not only in the information domain (motion planning through ZFT) but also in the energy domain (physical interaction through impedance), a key property that we exploit later for energy-based stiffness estimation (Section III-D).

C. Diffusion Model for reconstruction of sZFT

From the perspective of diffusion, the displacement Δx can be interpreted as noise corrupting the equilibrium pose $(\mathbf{p}_0, \mathbf{q}_0)$. The role of the Diffusion Model is to reconstruct the equilibrium pose by iteratively removing this noise. During training, the model learns to predict the difference between the observed pose (\mathbf{p}, \mathbf{q}) and the ground truth equilibrium pose, guided by the measured external wrench \mathbf{F}_{ext} (Figure 3). At inference, the model denoises Δx and outputs the reconstructed sZFT $(\hat{\mathbf{p}}_0, \hat{\mathbf{q}}_0)$.

It is important to distinguish between ZFT $(\mathbf{p}_0, \mathbf{q}_0)$ and sZFT $(\hat{\mathbf{p}}_0, \hat{\mathbf{q}}_0)$ in our formulation. The ZFT is the nominal Zero-Force Trajectory: a programmed equilibrium motion that remains unchanged in execution and can be generated by frame-based programming, imitation learning (for free-space motion [49], [50], with possible post-processing for contact tasks [51], [52]), or telemanipulation [53]. For deployment in the experiments of this paper, free-space trajectories were generated programmatically by chaining waypoints with minimum-jerk and *Spherical Linear Interpolation* (SLERP) [54], without any contact feedback. The code for ZFT generation is available on GitHub⁶.

The sZFT, in contrast, is not programmed. It is reconstructed by the Diffusion Model from the observed pose and external wrench and serves exclusively as input to stiffness estimation. Thus, while the ZFT prescribes the nominal equilibrium motion in the absence of contact, the sZFT provides

a denoised, contact-consistent equilibrium estimate for real-time impedance adaptation. The controller continues to track the ZFT as the nominal reference, incorporating the sZFT implicitly through stiffness modulation (Figure 4).

For example, when the robot encounters an unexpected obstacle such as a bumper (Figure 5, right), the planned ZFT drives it into contact, producing an external wrench. Conditioned on this wrench, the Diffusion Model reconstructs the sZFT: a shifted trajectory that is physically consistent with the contact. This reconstruction then forms the basis for updating stiffness and damping, enabling the robot to preserve the intended impedance behavior even as its motion adapts to the new environment.

Having illustrated the effect conceptually, we now formalize the denoising process, which can be expressed in translational and rotational noise components. For translations, the full noise is defined as

$$\mathbf{p}_{\text{noise}} = \mathbf{p} - \mathbf{p}_0. \quad (9)$$

During training, a fraction of this noise is added to the clean equilibrium pose via the noise scheduler (Section III-B), and the network is trained to predict it. At inference, the predicted noise $\hat{\mathbf{p}}_{\text{noise}}$ is subtracted from the observation to reconstruct the equilibrium position iteratively,

$$\hat{\mathbf{p}}_0 = \mathbf{p} - \hat{\mathbf{p}}_{\text{noise}}. \quad (10)$$

For rotations, the full noise is represented by the relative quaternion

$$\mathbf{q}_{\text{noise}} = \mathbf{q} \mathbf{q}_0^{-1}, \quad (11)$$

which encodes the rotational displacement between the observed quaternion \mathbf{q} and the equilibrium quaternion \mathbf{q}_0 . Partial training noise is injected to \mathbf{q}_0 using SLERP [54] (Section III-B), and the network is trained to predict $\hat{\mathbf{q}}_{\text{noise}}$. At inference, the equilibrium quaternion is reconstructed by

$$\hat{\mathbf{q}}_0 = \mathbf{q} \hat{\mathbf{q}}_{\text{noise}}^{-1}. \quad (12)$$

The reconstructed sZFT provides the essential input for energy-based stiffness estimation, which is the ratio between equilibrium displacement Δx and measured wrench \mathbf{F}_{ext} (eq.(7)). This enables stiffness modulation to be computed in the energy domain (Section III-D). In this sense, diffusion serves as the bridge between contact-rich (“noisy”) observed trajectories and impedance-based adaptation (Figure 4).

III. DIFFUSION-BASED IMPEDANCE LEARNING

A. Data Collection

All training data for Diffusion-Based Impedance Learning was collected through teleoperation with AVP, which provided ground truth sZFTs alongside measured wrenches and robot motion. Unlike demonstrations with manipulandums or other telemanipulation devices that are spatially restricted, this setup allowed unconstrained demonstrations. In practice, the operator’s hand pose tracked by AVP could move freely in space, unconstrained by physical objects, whereas the robot end-effector was constrained by actual contact with those same surfaces. This set-up enabled to capture both free space

⁶<https://github.com/StrokeAIRobotics/DiffusionBasedImpedanceLearning>

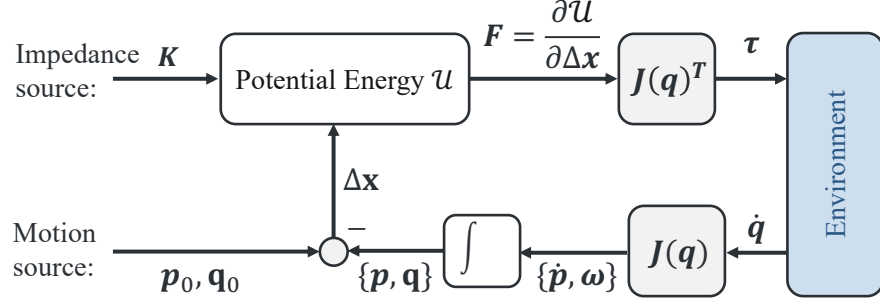


Fig. 2: Norton equivalent network of Impedance Control. The interaction is represented as the combination of a motion source and an impedance source. The displacement Δx is mapped through stiffness K to generate wrench, while the environment contributes external wrenches. This energy-based view ensures consistency between commanded motion and force response.



Fig. 3: Diffusion-based reconstruction of the simulated Zero-Force Trajectory (szFT). The observed pose $\{p, q\}$ together with the external wrench F_{ext} is treated as noise relative to the equilibrium $\{p_0, q_0\}$. The Diffusion Model iteratively denoises this input to reconstruct the equilibrium trajectory, which is then used in energy-based stiffness estimation.

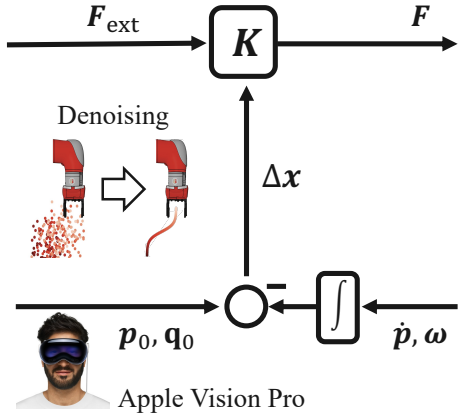


Fig. 4: Summary of Diffusion-Based Impedance Learning. Teleoperated demonstrations provide ground truth data for model training, which become corrupted by noise during interaction. The Diffusion Model reconstructs the szFT, which then, together with the external wrench F_{ext} , serves as input for energy-based stiffness estimation and adaptive Impedance Control.

motion and contact-induced deviations, which is important for applications that include transitions into and out of contact.

Two datasets were generated. The first consisted of a parkour-style scenario with multiple obstacles, including a bumper, circular target, ramp, and flat tabletop (Figure 5, right). A total of 17,457 samples were recorded. These data captured diverse contact interactions representative of unstructured environments.

The second dataset focused on robotic-assisted upper-limb rehabilitation tasks (Figure 5, left). A total of 55,838 samples were recorded. Eight healthy adults (4 female, 4 male; age 20–64 years; height 162–192 cm; weight 64–91 kg) performed movements derived from standard post-stroke protocols. Each task was executed under three conditions: (i) passive, where the robot guided the subject’s arm; (ii) cooperative, where subjects actively minimized interaction wrenches; and (iii) mixed, where both robot and subject contributed. The study was approved by MIT’s Committee on the Use of Humans as Experimental Subjects (COUHES), with informed consent obtained from all participants. This dataset was used to train the model presented in this paper; however, the deployment of upper-limb rehabilitation applications is part of a separate project and is not reported here.

B. Noise Scheduling

For the denoising of the Diffusion Model, the maximum noise magnitude was computed separately for translations and rotations, and a variational noise schedule was applied across diffusion steps.

1) *Translations*: For translations, the deviation between the observed end-effector position p and the ground-truth ZFT p_0 was treated as noise. Additional zero-mean Gaussian noise $\epsilon_{\text{gauss}} \sim \mathcal{N}(0, \sigma^2 I)$ was injected during training to improve generalization and prevent overfitting [55]. The translational noise for the model is defined as

$$\text{noise}_t = p - p_0 + \epsilon_{\text{gauss}}, \quad (13)$$

with perturbed positions computed as

$$p_{\text{noise}} = p_0 + \beta_t \cdot \text{noise}_t, \quad (14)$$

where β_t is the noise scaling factor at diffusion step t .

2) *Rotations*: In our robot controller, orientations are represented with unit quaternions q . Injecting noise, as in the translational case, would violate the unit-norm constraint and distort the geometry of rotations. To address this, we introduce a SLERP-based [54] noise scheduler that perturbs quaternions directly on the unit sphere. This approach preserves valid orientations, provides perturbations consistent with geodesics, and allows rotational noise to be scheduled smoothly across



Fig. 5: Examples of teleoperated demonstrations used for training. (Left) Physical therapy dataset with robotic-assisted upper-limb tasks. (Right) Parkour dataset with free-space and contact-rich motions across obstacles.

diffusion steps. To our knowledge, this is the first physically-consistent noise scheduler for rotations in robotics, formulated directly on a global representation of rotations [47].

The SLERP operation is illustrated in Figure 6. The interpolation between two quaternions \mathbf{q}_a and \mathbf{q}_b is defined as

$$\text{SLERP}(\mathbf{q}_a, \mathbf{q}_b; \mu) = \frac{\sin((1 - \mu)\Omega)}{\sin(\Omega)} \mathbf{q}_a + \frac{\sin(\mu\Omega)}{\sin(\Omega)} \mathbf{q}_b, \quad (15)$$

where $\Omega = \arccos(\langle \mathbf{q}_a, \mathbf{q}_b \rangle)$ is the angle between \mathbf{q}_a and \mathbf{q}_b , and $\mu \in [0, 1]$ is the interpolation factor.

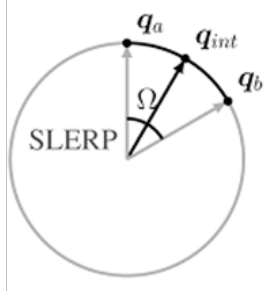


Fig. 6: Rotational noise scheduling with spherical linear interpolation (SLERP) [54]. Perturbed quaternions stay on the unit sphere, enabling geometry-consistent noise injection and removal.

C. Model Selection to reconstruct sZFT

Our model selection was guided by two initial requirements: (i) sufficient accuracy in reconstructing both translational and rotational components and (ii) a small model capacity, suitable for real-time deployment. To evaluate this trade-off, we varied hidden dimensions, number of layers, attention heads, and loss-weighting strategies. Performance was assessed using translational error (positional loss in mm) and rotational error (angular magnitude θ about unit-axis and unit-axis deviation α in degrees).

Figure 7 provides a graphical representation of the rotational losses, illustrating the decomposition into axis deviation α_{error} and magnitude error θ_{error} .

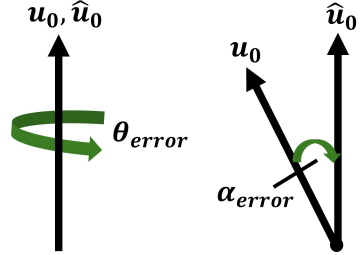


Fig. 7: Graphical representation of rotational losses, showing axis deviation α_{error} and magnitude error θ_{error} .

Our initial requirements were 2 mm for the translational error and 2.8° (half of the small-angle approximation) for the angular error and unit-axis deviation. These values were determined heuristically based on other contact-rich experiments [56].

Table II reports the results for the Transformer-based Diffusion Model on the parkour dataset. The configuration with 512 hidden dimensions, 4 attention heads, and 6 layers achieved the best balance between accuracy and efficiency, with positional error of 0.994 mm, θ error of 0.249°, and α error of 0.003°. Increasing the loss weight of the θ component (factor 5) yielded marginal improvements in rotational accuracy ($\theta = 0.240^\circ$, $\alpha = 0.003^\circ$) without degrading translational fidelity.

A notable result was that retraining this model on a combined dataset of parkour and robotic-assisted therapy motions further improved accuracy (positional error 0.883 mm, θ error 0.233°, α error 0.002°). Importantly, the two datasets were collected with different tools and inertial properties (lightweight tool for parkour and a 600 g prosthetic hand for physical therapy) yet the model compensated for these differences without explicit training. This robustness highlights the ability of Diffusion-Based Impedance Learning to generalize across diverse physical environments. The selected architecture was ultimately adopted as the final model because it satisfied the accuracy requirements while remaining small enough for real-time torque control.

Another notable finding of this work is the small amount of

TABLE II: Transformer-based Diffusion Model results (parkour dataset). The selected model (highlighted) combines high accuracy with low computational complexity.

Hidden Dim	Heads	Layers	θ Loss [deg]	α Loss [deg]	Positional Loss [mm]
512	4	4	0.307	0.004	1.047
512	4	6	0.249	0.003	0.994
512	8	4	0.282	0.004	1.030
512	8	6	0.286	0.003	0.989
1024	4	4	0.228	0.003	1.033
1024	4	6	0.224	0.003	1.033
1024	8	4	0.227	0.003	1.016
1024	8	6	0.288	0.004	1.057

training data required. The model already showed strong performance on the parkour dataset with only tens of thousands of samples. In our case, 17,457 samples at a controller rate of 0.005 s correspond to just 1.5 hours of demonstration. This is in contrast to image-based Diffusion Models, which often require hundreds to thousands of demonstrations to achieve high-quality results [53], [57].

D. Energy-based Stiffness Estimation

Based on the sZFT, we compute stiffness by equating virtual elastic energy stored in a virtual spring to measured work performed by external wrenches.

For deployment, a user can specify baseline translational and rotational stiffness values. The Diffusion Model predicts the sZFT, i.e., the equilibrium pose consistent with the current interaction wrench. Rather than altering the programmed ZFT, we preserve the intended interactive behavior by computing nonnegative reduction terms $k_{t,i}^*$ and $k_{r,i}^*$, which are subtracted from the predefined baseline stiffnesses $K_{t,i,\max}$ and $K_{r,i,\max}$, thereby keeping the effective stiffness relative to the sZFT constant:

$$k_{t,i} = K_{t,i,\max} - k_{t,i}^*, \quad (16a)$$

$$k_{r,i} = K_{r,i,\max} - k_{r,i}^*. \quad (16b)$$

Here, $i \in \{x, y, z\}$ denotes the translational or rotational axis. In our experiments, the baseline stiffness values were set deliberately high ($K_{t,i,\max} = 800$ N/m, $K_{r,i,\max} = 150$ Nm/rad) to ensure that the robot had sufficient energy for all tasks, while allowing the model to autonomously reduce stiffness when contact occurred.

1) *Translations*: For translations, the displacement is defined as $e_t = p - p_0$. The elastic energy $E_t \in \mathbb{R}$ of a virtual translational spring is

$$E_t^{\text{spring}} = \frac{1}{2} \mathbf{K}_t \|e_t\|^2. \quad (17)$$

Here, $\|\cdot\|$ denotes the Euclidean norm. The work done by the external force $f_{\text{ext}} \in \mathbb{R}^3$ along the displacement e_t is given by the inner product $\langle \cdot, \cdot \rangle$:

$$E_t^{\text{work}} = \langle f_{\text{ext}}, e_t \rangle. \quad (18)$$

Equating eq. (17) with eq. (18) yields the translational stiffness contribution

$$k_t^* = \frac{2 \langle f_{\text{ext}}, e_t \rangle}{\|e_t\|^2}. \quad (19)$$

To avoid oscillatory behavior, a damping term proportional to velocity error is introduced:

$$\tilde{e}_t = \kappa_t e_t - \gamma_t \dot{e}_t, \quad (20)$$

where κ_t is a unit translational stiffness and γ_t a damping coefficient (Appendix A-C).

2) *Rotations*: For rotations, the unit axis-angle representation $e_r = u_0 \theta_0$ is used (eq. (5)). The corresponding elastic energy $E_r \in \mathbb{R}$ of the virtual rotational spring is

$$E_r^{\text{spring}} = \frac{1}{2} \mathbf{K}_r \|e_r\|^2. \quad (21)$$

The work done by the external moment $\mathbf{m}_{\text{ext}} \in \mathbb{R}^3$ about the rotational displacement e_r can be calculated by

$$E_r^{\text{work}} = \langle \mathbf{m}_{\text{ext}}, e_r \rangle. \quad (22)$$

Equating eq. (21) with eq. (22) results in the rotational stiffness contribution

$$k_r^* = \frac{2 \langle \mathbf{m}_{\text{ext}}, e_r \rangle}{\|e_r\|^2}. \quad (23)$$

Dynamic effects are addressed by augmenting the error with a damping term:

$$\tilde{e}_r = \kappa_r e_r - \gamma_r \omega, \quad (24)$$

where κ_r is a unit rotational stiffness, ω is the angular velocity, and γ_r a damping coefficient (Appendix A-C).

3) *Algorithm*: Algorithm 1 summarizes the procedure of the stiffness estimation. Stiffness was computed over a sliding window of 16 samples at 200 Hz (80 ms), which was sufficient given that the tasks were not highly dynamic. Thresholds of 1 N for force and 1 Nm for moment were applied, and values below these limits were ignored to suppress phases of low interaction.

4) *Directional adaptation*: For deployment of our model in real world experiments, the energy-based estimator was extended with a directional adaptation step. A uniform reduction of stiffness in response to external perturbations can prevent task execution, e.g., the end-effector may stop when encountering an obstacle. To avoid this problem, stiffness was modulated according to the directional relevance of each axis with respect to the model-generated sZFT. The alignment factors below are defined relative to p_0 and $u_0 \theta_0$ contained in e_t and e_r , which are outputs of the Diffusion Model. Hence, the adaptation mechanism depended critically on the reconstructed sZFT: if the nominal free-space ZFT were used directly, the alignment factors would not reflect the equilibrium under contact, and directional adaptation would fail (Section IV).

Algorithm 1 Energy-Based Stiffness Estimation

```

1: Input:  $e_t, \dot{e}_t, \ddot{e}_t, \omega, f_{\text{ext}}, m_{\text{ext}}, \kappa_t, \kappa_r, \gamma_t, \gamma_r$ ,
    $f_{\text{thres}}, m_{\text{thres}}, K_{t,\text{max}}, K_{r,\text{max}}, \varepsilon$ 
2: for  $i \in \{x, y, z\}$  do
3:    $\tilde{e}_{t,i} \leftarrow \kappa_t e_{t,i} - \gamma_t \dot{e}_{t,i}$ 
4:   if  $|f_i| < f_{\text{thres}}$  or  $\tilde{e}_{t,i}^2 < \varepsilon$  then
5:      $k_{t,i}^* \leftarrow 0$ 
6:   else
7:      $k_{t,i}^* \leftarrow \frac{2 f_i \tilde{e}_{t,i}}{\tilde{e}_{t,i}^2 + \varepsilon}$ 
8:      $k_{t,i}^* \leftarrow \max(0, k_{t,i}^*)$ 
9:   end if
10:   $K_{t,i} \leftarrow \text{clip}(K_{t,\text{max},i} - k_{t,i}^*, 0, K_{t,\text{max},i})$ 
11:   $\tilde{e}_{r,i} \leftarrow \kappa_r e_{r,i} - \gamma_r \omega_i$ 
12:  if  $|m_i| < m_{\text{thres}}$  or  $\tilde{e}_{r,i}^2 < \varepsilon$  then
13:     $k_{r,i}^* \leftarrow 0$ 
14:  else
15:     $k_{r,i}^* \leftarrow \frac{2 m_i \tilde{e}_{r,i}}{\tilde{e}_{r,i}^2 + \varepsilon}$ 
16:     $k_{r,i}^* \leftarrow \max(0, k_{r,i}^*)$ 
17:  end if
18:   $K_{r,i} \leftarrow \text{clip}(K_{r,\text{max},i} - k_{r,i}^*, 0, K_{r,\text{max},i})$ 
19: end for
20: Output:  $K_t, K_r$ 

```

For translations, the alignment factor

$$\psi_{t,i} = \frac{|e_{t,i}|}{\|e_t\|}, \quad i \in \{x, y, z\} \quad (25)$$

quantifies the contribution of each axis to the intended displacement. Analogously, for rotations we define

$$\psi_{r,i} = \frac{|e_{r,i}|}{\|e_r\|}, \quad i \in \{x, y, z\}. \quad (26)$$

The relative translational and rotational factors $\rho_{t,i}$ and $\rho_{r,i}$ ensure that stiffness is decreased more strongly in directions that contribute little to the desired motion, while remaining close to the baseline stiffness along task-relevant axes:

$$\rho_{t,i} = 1 - \psi_{t,i}, \quad (27a)$$

$$\rho_{r,i} = 1 - \psi_{r,i}. \quad (27b)$$

The final adapted stiffness values $k_{t,i}$ and $k_{r,i}$ were implemented as

$$k_{t,i} = K_{t,i,\text{max}} - \rho_{t,i} k_{t,i}^*, \quad (28a)$$

$$k_{r,i} = K_{r,i,\text{max}} - \rho_{r,i} k_{r,i}^*. \quad (28b)$$

As will be shown in the next section, this mechanism allowed the robot to move smoothly over obstacles in the parkour task and to achieve successful in peg-in-hole insertion.

IV. DEPLOYMENT OF DIFFUSION MODEL ON REAL ROBOT

The model was deployed in two robotic use-cases designed to evaluate its performance in contact-rich scenarios. We deliberately focus on Impedance Control rather than motion generation, since many real world applications require active compliance, e.g., final assembly tasks where vision is occluded

and only tactile sensing is available. The first was a parkour-style task requiring continuous interaction while traversing unknown obstacles. The second was a peg-in-hole insertion task with increasing geometric complexity.

The experiments were conducted on a KUKA LBR iiwa with seven DOFs, using KUKA's Fast Robot Interface (FRI) for torque control with 5 ms sample time. Built-in gravity and Coriolis/centrifugal compensation remained active throughout. Kinematic and dynamic matrices were computed via the Exp[licit]-FRI interface⁷ [58]. The external wrenches were acquired with an ATI Gamma force/torque transducer, mounted on the robot flange. The code is publicly available on our GitHub repository⁸.

In both experiments, we compared a task-space Impedance Controller (Appendix A) with constant stiffness values against our proposed diffusion-based directional stiffness adaptation. For all trials, baseline translational stiffness was set to 800 $\frac{\text{N}}{\text{m}}$ and baseline rotational stiffness to 150 $\frac{\text{Nm}}{\text{rad}}$. The same damping design was applied throughout (Appendix A-C).

All workpieces were fabricated with a PRUSA i3 MK3 3D printer using PLA filament, and CAD models are available on our GitHub repository. Demonstration videos of both experiments are provided on the project website⁹.

A. Parkour

The first experiment was a parkour-style task in which the robot had to traverse multiple obstacles with continuous contact. The nominal parkour ZFT was generated from a sequence of key configurations connected via minimum-jerk and SLERP interpolation (see code on GitHub).

To protect the setup, stop conditions of $\|v\| = 0.24 \frac{\text{m}}{\text{s}}$ and $\|f_{\text{ext}}\| = 20 \text{ N}$ were defined. The constant-stiffness controller already failed at the first obstacle: the end-effector was stopped by the bumper, energy accumulated in the virtual spring, and once this energy was released the end-effector accelerated into the velocity stop condition. Forces of up to 15 N were observed. In contrast, with diffusion-based impedance adaptation, the robot traversed all obstacles smoothly, i.e., not violating the velocity or force stop conditions. The stiffness adaptation mechanism prevented jamming in directions inconsistent with the ZFT while preserving rigidity along task-relevant axes.

The videos of the experiments with constant stiffness and Diffusion-Based Impedance Learning can be found on our project website.

Figure 8 shows the measured external wrenches together with the commanded translational and rotational stiffness values for the Diffusion-Based Impedance Learning. The bottom plots illustrate the relative translational and rotational factors (Equation (27)) that modulate the stiffness based on the contribution of each axis to the ZFT.

During the entire motion, stiffness values changed dynamically in response to external wrenches. This continuous adaptation reflected the underlying Diffusion-Based Impedance Learning, which enabled the robot to remain compliant when

⁷<https://GitHub.com/explicit-robotics/Explicit-FRI>

⁸<https://github.com/StrokeAIRobotics/DiffusionBasedImpedanceLearning>

⁹<https://strokeairobotics.github.io/DiffusionBasedImpedanceLearning>

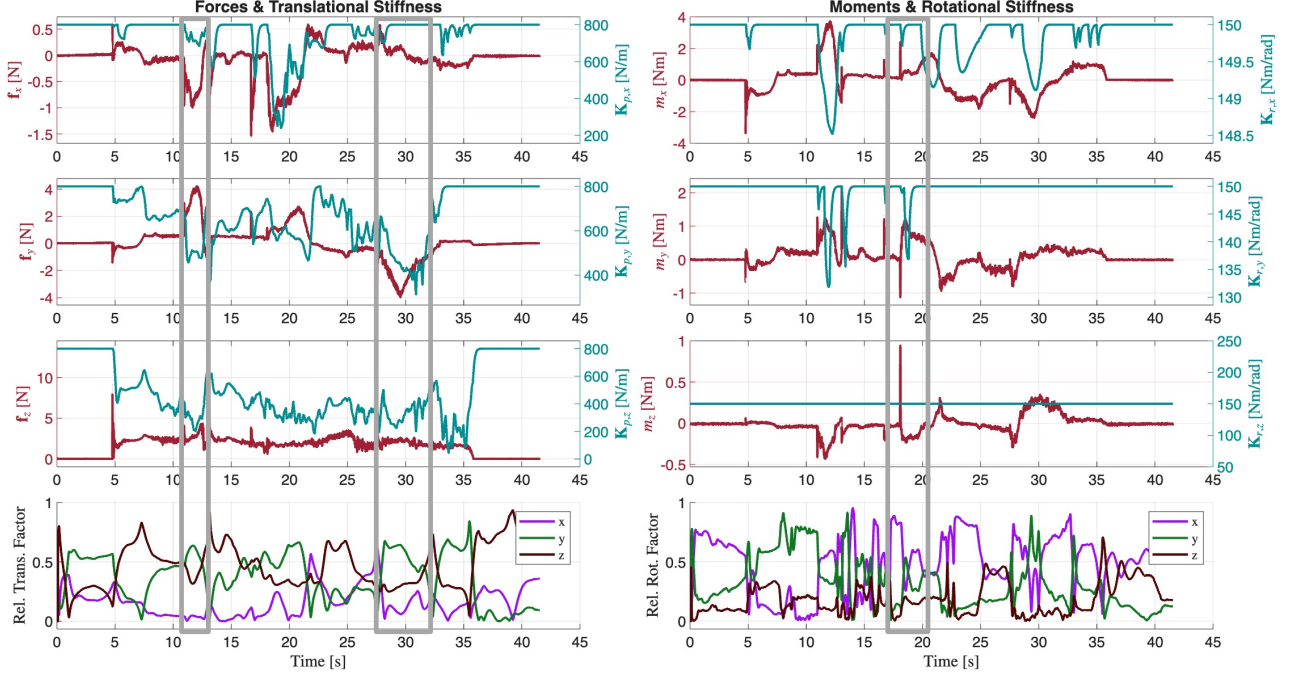


Fig. 8: Measured external wrenches and commanded translational and rotational stiffness during the parkour experiment with stiffness adaptation. All quantities are expressed in the robot base frame. The lower plots show the relative translational and rotational factors and their influence on stiffness modulation. The highlighted gray regions illustrate stiffness reduction in response to external wrenches, governed by the relative translational and rotational factors.

unexpected contact occurred while maintaining sufficient stiffness to progress through the parkour.

Translational stiffness adapted asymmetrically depending on the directional contribution of forces. Around 12–13 s, similar forces appeared along both the y - and z -axes. Nevertheless, $K_{p,z}$ was reduced more strongly (to about 200 N/m) than $K_{p,y}$ (remaining near 500 N/m). A similar effect is visible near 30 s: while f_y reached about 4 N with stiffness near 400 N/m, f_z was only 2 N yet stiffness dropped to about 200 N/m. These findings confirm that stiffness reduction was not simply proportional to force magnitude but was determined by the relative translational factors and their alignment with the sZFT.

Rotational stiffness also adapted directionally, with reductions depending on which axis contributed less to the sZFT. Around 19 s, moments appeared simultaneously about the x - and y -axes. Despite higher magnitudes about the x -axis, the stiffness $K_{r,y}$ was reduced more strongly, showing that y -axis rotations were less important for the intended trajectory. This selective modulation allowed the robot to maintain stability while avoiding unnecessary resistance to contact.

B. Peg-In-Hole Insertion

The second experiment was a peg-in-hole insertion task with three different peg types: cylindrical, square, and star pegs. The nominal clearance between each peg and its corresponding hole was 0.14 mm for the square peg and 0.20 mm for the circular and star pegs. All workpieces were fabricated with the same printer setup as for the parkour experiment. For all trials, task success was defined as completely inserting the peg.

As with the parkour experiment, nominal trajectories were constructed by minimum-jerk interpolation between 3 key robot poses: approach and contact, final insertion, and retreat.

The three peg types represent increasing geometric complexity. The cylindrical peg is rotationally symmetric, which makes the final orientation about the end-effector z -axis irrelevant. In contrast, the square and star pegs require precise alignment with an increasing number of edges, which significantly increases task complexity. This was confirmed by the experiments with constant stiffness values: the cylindrical peg was inserted successfully in 30/30 trials, the square peg in 4/30 trials, and the star peg in none of the 30 trials.

In contrast, Diffusion-Based Impedance Learning achieved a 30/30 success rate for all three peg types. These results highlight that with increasing insertion complexity, more advanced strategies such as our diffusion-based approach become essential. The outcome is particularly notable because the training data included only parkour and upper-limb rehabilitation data (Section III-A) and no peg-in-hole demonstrations.

The videos of the experiments with constant stiffness and Diffusion-Based Impedance Learning can be found on our project website¹⁰.

Figure 9 shows the stiffness adaptation for the star peg. Results for the other two pegs are provided in Appendix C. During all experiments, force and moment thresholds were set to 1 N and 1 Nm, respectively.

As illustrated in Figure 9, stiffness values were reduced in response to external wrenches, with the amount of reduction

¹⁰<https://strokeairobotics.github.io/DiffusionBasedImpedanceLearning>

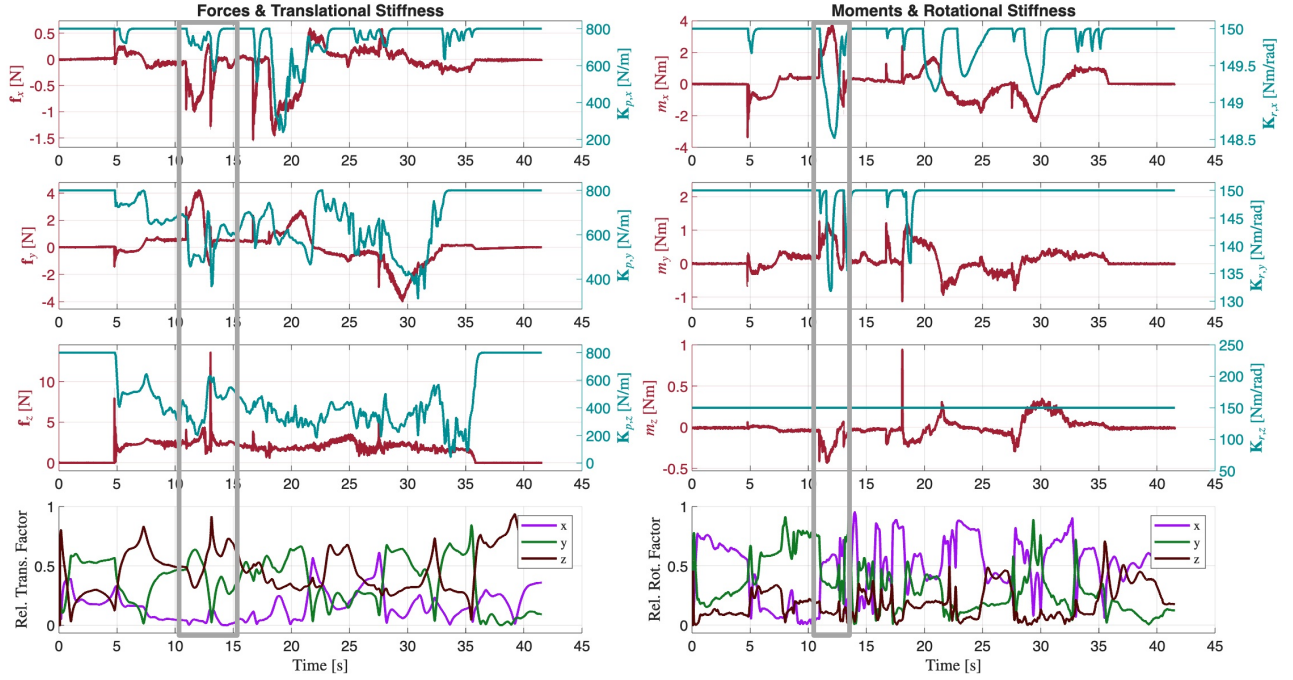


Fig. 9: Measured external wrenches and commanded translational and rotational stiffness during the star peg insertion experiment. All quantities are expressed in the robot base frame. The lower plots show the directional motion factors for translation and rotation and their influence on stiffness modulation. The highlighted gray region illustrates stiffness reduction in response to external wrenches, governed by the relative translational and rotational factors.

governed by the relative translational and rotational factors. At around 11 s, forces of 3–4 N appeared along both the y - and z -axes. Nevertheless, the stiffness $K_{p,z}$ was reduced more strongly than $K_{p,y}$ because the relative translational factor in z was lower. At around 13 s, even though a force peak of 14 N occurred along z , the stiffness was only marginally reduced since the relative translational factor approached 1.

Due to the high stiffness reduction of translations, the external moments remained small (below 4 Nm). The effect of the relative rotational factor can be seen for rotations about the x - and y -axes near 12 s. A moment of 4 Nm about the x -axis and 1 Nm about the y -axis resulted in a stronger reduction of $K_{r,y}$ than $K_{r,x}$, reflecting the higher contribution of y -axis rotations to the sZFT.

Ablation study. In addition to the two main controllers, we evaluated uniform stiffness adaptation and directional adaptation computed from the nominal ZFT (i.e., the commanded free-space trajectory). Uniform stiffness adaptation failed in both scenarios: the parkour traversal was blocked at the first obstacles, and none of the peg-in-hole insertions succeeded. Directional adaptation from the nominal ZFT also failed in contact-rich settings: in parkour, the robot hit the safety bounds and stopped, while in peg-in-hole tasks it achieved 30/30 success only for the cylindrical peg but failed for both square and star pegs. These results confirm that directional factors must be derived from the reconstructed, contact-consistent sZFT rather than from the nominal ZFT in order for impedance adaptation to succeed.

V. DISCUSSION

The experimental results confirm the central goal of this work: enabling robust contact-rich manipulation by bridging the information and energy domains and unifying state-of-the-art generative AI algorithms with model-based control. In particular, the success of peg-in-hole insertions with unseen geometries demonstrates that sZFT reconstruction generalizes equilibrium adaptation beyond the training distribution.

Compared to prior learning-based approaches, our framework explicitly incorporates energy consistency, enabling stable impedance adaptation even under contact. Conversely, compared to traditional model-based Impedance Controllers, it gains adaptability by reconstructing equilibrium trajectories directly from data. This ability to bridge domains accounts for the strong performance observed in unstructured environments.

A key element of the framework is directional stiffness adaptation. This mechanism is generic and can be tailored to applications in other domains. One example is robotic-assisted upper-limb therapy, where stiffness must remain high along non-movement directions to ensure patient safety, while stiffness along the intended movement direction should adapt depending on whether the patient can execute the motion independently. In such settings, our framework could provide both safety and flexibility, adjusting assistance in real time.

At present, the adaptive Impedance Controller outputs diagonal, positive semidefinite stiffness matrices. This design simplifies analysis and implementation but omits cross-coupling effects that have proven beneficial in traditional solutions such as remote-center compliance (RCC) devices [59], [60]. For

more complex assembly tasks, integrating coupled stiffness parameters may further enhance robustness and alignment accuracy. Exploring this extension is an important direction for future work.

The proposed approach guarantees passivity when stiffness is reduced: lowering stiffness dissipates stored potential energy and ensures that interaction with a passive environment remains output strictly passive. However, when stiffness is increased back toward the baseline, passivity is not generally guaranteed, as such changes can inject additional energy whenever displacements are nonzero. In these cases, the controller can be combined with our earlier work on passive impedance shaping [61] to enforce strict passivity.

Overall, our findings demonstrate that Diffusion-Based Impedance Learning is highly effective in the experimental setups investigated. While this provides strong evidence for the viability of the approach, further studies across a wider range of tasks and environments are needed to fully establish its generality. Nevertheless, the framework offers a promising design principle for stable, safe, and adaptable robot interaction in other domains like industrial assembly, physical Human-Robot Interaction, and robotic-assisted therapy.

VI. CONCLUSION

This work introduced *Diffusion-Based Impedance Learning*, a framework that unifies generative trajectory models in the information domain with adaptive impedance regulation in the energy domain. By reconstructing simulated Zero-Force Trajectories (sZFTs) from contact-perturbed displacements and external wrench signals, the method enables real-time impedance adaptation for contact-rich manipulation.

The framework consistently outperformed fixed and heuristic strategies in experiments on a KUKA LBR iiwa. It enabled smooth traversal of obstacle-rich parkour environments where conventional Impedance Control failed, and achieved 30/30 success rates in cylindrical, square, and star peg-in-hole insertions without any task-specific demonstrations.

Beyond these results, Diffusion-Based Impedance Learning establishes a general interface between learning and model-based control. It extends the role of generative models from visuomotor trajectory planning to physical interaction.

Looking ahead, we aim to extend this framework from single-arm to dual-arm setups and to human–robot collaborative systems. Embedding Diffusion-Based Impedance Learning in hierarchical architectures that couple high-level visuomotor policies with low-level impedance regulation could yield robots that both plan intelligently and interact safely in unstructured, human-centered environments. Ultimately, such systems may handle the variability of industrial assembly lines, support cooperative human–robot tasks, and provide personalized assistance in clinical care.

ACKNOWLEDGEMENTS

We gratefully acknowledge the support of KUKA, an international leader in automation solutions, and specifically thank them for providing the KUKA robots used in our experiments.

REFERENCES

- [1] N. Hogan, “Stable execution of contact tasks using impedance control,” in *Proceedings. 1987 IEEE International Conference on Robotics and Automation*, vol. 4. IEEE, 1987, pp. 1047–1054.
- [2] J. Lachner, F. Allmendinger, E. Hobert, N. Hogan, and S. Stramigioli, “Energy budgets for coordinate invariant robot control in physical human–robot interaction,” *The International Journal of Robotics Research*, vol. 40, no. 8-9, pp. 968–985, Aug. 2021.
- [3] S. Stramigioli, Ed., *Energy-Aware Robotics*, ser. Mathematical Control Theory I. Switzerland: Springer International Publishing, 2015, vol. 461.
- [4] N. Hogan, “A general actuator model based on nonlinear equivalent networks,” *IEEE/ASME Transactions on Mechatronics*, vol. 19, no. 6, pp. 1929–1939, 2014.
- [5] ———, “Impedance control—an approach to manipulation. i-theory. ii-implementation. iii-applications,” *ASME Journal of Dynamic Systems and Measurement Control B*, vol. 107, pp. 1–24, 1985.
- [6] M. Posa, C. Cantu, and R. Tedrake, “A direct method for trajectory optimization of rigid bodies through contact,” *The International Journal of Robotics Research*, vol. 33, no. 1, pp. 69–81, 2014.
- [7] Z. Manchester and S. Kuindersma, “Variational contact-implicit trajectory optimization,” in *Robotics Research: The 18th International Symposium ISRR*. Springer, 2020, pp. 985–1000.
- [8] T. Pang, H. T. Suh, L. Yang, and R. Tedrake, “Global planning for contact-rich manipulation via local smoothing of quasi-dynamic contact models,” *IEEE Transactions on Robotics*, 2023.
- [9] T. Marcucci, R. Deits, M. Gabiccini, A. Bicchi, and R. Tedrake, “Approximate hybrid model predictive control for multi-contact push recovery in complex environments,” in *2017 IEEE-RAS 17th international conference on humanoid robotics (Humanoids)*. IEEE, 2017, pp. 31–38.
- [10] F. R. Hogan and A. Rodriguez, “Reactive planar non-prehensile manipulation with hybrid model predictive control,” *The International Journal of Robotics Research*, vol. 39, no. 7, pp. 755–773, 2020.
- [11] M. Anitescu and F. A. Potra, “Formulating dynamic multi-rigid-body contact problems with friction as solvable linear complementarity problems,” *equivalentlinear Dynamics*, vol. 14, pp. 231–247, 1997.
- [12] A. Aydinoglu and M. Posa, “Real-time multi-contact model predictive control via admmm,” in *2022 International Conference on Robotics and Automation (ICRA)*. IEEE, 2022, pp. 3414–3421.
- [13] H. J. T. Suh, T. Pang, and R. Tedrake, “Bundled gradients through contact via randomized smoothing,” *IEEE Robotics and Automation Letters*, vol. 7, no. 2, pp. 4000–4007, 2022.
- [14] H. J. T. Suh, T. Pang, T. Zhao, and R. Tedrake, “Dexterous contact-rich manipulation via the contact trust region,” 2025. [Online]. Available: <https://arxiv.org/abs/2505.02291>
- [15] E. Theodorou, J. Buchli, and S. Schaal, “A generalized path integral control approach to reinforcement learning,” *The Journal of Machine Learning Research*, vol. 11, pp. 3137–3181, 2010.
- [16] M. Kalakrishnan, S. Chitta, E. Theodorou, P. Pastor, and S. Schaal, “Stomp: Stochastic trajectory optimization for motion planning,” in *2011 IEEE international conference on robotics and automation*. IEEE, 2011, pp. 4569–4574.
- [17] F. Stulp, E. A. Theodorou, and S. Schaal, “Reinforcement learning with sequences of motion primitives for robust manipulation,” *IEEE Transactions on robotics*, vol. 28, no. 6, pp. 1360–1370, 2012.
- [18] G. Williams, A. Aldrich, and E. A. Theodorou, “Model predictive path integral control: From theory to parallel computation,” *Journal of Guidance, Control, and Dynamics*, vol. 40, no. 2, pp. 344–357, 2017.
- [19] C. Chi, S. Feng, Y. Du, Z. Xu, E. Cousineau, B. Burchfiel, and S. Song, “Diffusion policy: Visuomotor policy learning via action diffusion,” *arXiv preprint arXiv:2303.04137*, 2023.
- [20] M. Braun, N. Jaquier, L. Rozo, and T. Asfour, “Riemannian flow matching policy for robot motion learning,” 10 2024, pp. 5144–5151.
- [21] F. Zhang and M. Gienger, “Affordance-based robot manipulation with flow matching,” 2025. [Online]. Available: <https://arxiv.org/abs/2409.01083>
- [22] M. Shridhar, L. Manuelli, and D. Fox, “Perceiver-actor: A multi-task transformer for robotic manipulation,” in *Conference on Robot Learning (CoRL)*, 2022. [Online]. Available: <https://arxiv.org/abs/2209.05451>
- [23] M. J. Kim, K. Pertsch, S. Karamcheti, T. Xiao, A. Balakrishna, S. Nair, R. Rafailov, E. Foster, G. Lam, P. Sanketi, Q. Vuong, T. Kollar, B. Burchfiel, R. Tedrake, D. Sadigh, S. Levine, P. Liang, and C. Finn, “Open-vla: An open-source vision-language-action model,” *arXiv preprint arXiv:2406.09246*, 2024.

[24] T. L. Team, J. Barreiros, A. Beaulieu, A. Bhat, R. Cory, E. Cousineau, H. Dai, C.-H. Fang, K. Hashimoto, M. Z. Irshad, M. Itkina, N. Kuppuswamy, K.-H. Lee, K. Liu, D. McConachie, I. McMahon, H. Nishimura, C. Phillips-Grafflin, C. Richter, P. Shah, K. Srinivasan, B. Wulfe, C. Xu, M. Zhang, A. Alspach, M. Angeles, K. Arora, V. C. Guizilini, A. Castro, D. Chen, T.-S. Chu, S. Creasey, S. Curtis, R. Denitto, E. Dixon, E. Dusel, M. Ferreira, A. Goncalves, G. Gould, D. Guoy, S. Gupta, X. Han, K. Hatch, B. Hathaway, A. Henry, H. Hochsztien, P. Horgan, S. Iwase, D. Jackson, S. Karamchetti, S. Keh, J. Masterjohn, J. Mercat, P. Miller, P. Mitiguy, T. Nguyen, J. Nimmer, Y. Noguchi, R. Ong, A. Onol, O. Pfannenstiehl, R. Poyner, L. P. M. Rocha, G. Richardson, C. Rodriguez, D. Seale, M. Sherman, M. Smith-Jones, D. Tago, P. Tokmakov, M. Tran, B. V. Hoorick, I. Vasiljevic, S. Zakharov, M. Zolotas, R. Ambrus, K. Fetzer-Borelli, B. Burchfiel, H. Kress-Gazit, S. Feng, S. Ford, and R. Tedrake, “A careful examination of large behavior models for multitask dexterous manipulation,” 2025. [Online]. Available: <https://arxiv.org/abs/2507.05331>

[25] Y. Hou, Z. Liu, C. Chi, E. Cousineau, N. Kuppuswamy, S. Feng, B. Burchfiel, and S. Song, “Adaptive compliance policy: Learning approximate compliance for diffusion guided control,” *arXiv preprint arXiv:2410.09309*, 2025.

[26] K. Li, X. Xiong, A. Wang, Y. Qu, and Y. Lou, “Implicit euler discrete-time set-valued admittance control for impact-contact force control,” *IEEE/ASME Transactions on Mechatronics*, pp. 1–12, 2024.

[27] Y. Park and P. Agrawal, “Using apple vision pro to train and control robots,” 2024. [Online]. Available: <https://github.com/Improbable-AI/VisionProTeleop>

[28] M. Janner, Y. Du, J. B. Tenenbaum, and S. Levine, “Planning with diffusion for flexible behavior synthesis,” in *Proceedings of the 39th International Conference on Machine Learning (ICML)*, 2022.

[29] A. Nichol and P. Dhariwal, “Improved denoising diffusion probabilistic models,” *arXiv preprint arXiv:2102.09672*, 2021.

[30] J. Ho, A. Jain, and P. Abbeel, “Denoising diffusion probabilistic models,” *arXiv preprint arXiv:2006.11239*, 2020.

[31] J. Sohl-Dickstein, E. Weiss, N. Maheswaranathan, and S. Ganguli, “Deep unsupervised learning using nonequilibrium thermodynamics,” in *Proceedings of the 32nd International Conference on Machine Learning*, ser. Proceedings of Machine Learning Research, F. Bach and D. Blei, Eds., vol. 37. Lille, France: PMLR, 07–09 Jul 2015, pp. 2256–2265.

[32] P. Holderith and E. Erives, “An introduction to flow matching and diffusion models,” *arXiv preprint arXiv:2506.02070*, 2025.

[33] X. Liu, K. Y. Ma, C. Gao, and M. Z. Shou, “Diffusion models in robotics: A survey,” *TechRxiv*, April 2025.

[34] U. A. Mishra and Y. Chen, “Reorientendiff: Diffusion model based reorientation for object manipulation,” *arXiv preprint arXiv:2303.12700*, 2023.

[35] J. Song, C. Meng, and S. Ermon, “Denoising diffusion implicit models,” *arXiv preprint arXiv:2010.02502*, 2020.

[36] R. Wolf, Y. Shi, S. Liu, and R. Rayyes, “Diffusion models for robotic manipulation: A survey,” *arXiv preprint arXiv:2504.08438*, 2025.

[37] A. Vaswani, N. Shazeer, N. Parmar, J. Uszkoreit, L. Jones, A. N. Gomez, Ł. Kaiser, and I. Polosukhin, “Attention is all you need,” in *Advances in Neural Information Processing Systems (NeurIPS)*, vol. 30, 2017.

[38] Y. Liang, H. Wen, Y. Nie, Y. Jiang, M. Jin, D. Song, S. Pan, and Q. Wen, “Foundation models for time series analysis: A tutorial and survey,” in *Proceedings of the 30th ACM SIGKDD Conference on Knowledge Discovery and Data Mining*, ser. KDD ’24. ACM, Aug. 2024, p. 6555–6565.

[39] A. Dosovitskiy, L. Beyer, A. Kolesnikov, D. Weissenborn, X. Zhai, T. Unterthiner, M. Dehghani, M. Minderer, G. Heigold, S. Gelly, J. Uszkoreit, and N. Houlsby, “An image is worth 16x16 words: Transformers for image recognition at scale,” in *International Conference on Learning Representations*, 2021.

[40] A. Jaegle, F. Gimeno, A. Brock, O. Vinyals, A. Zisserman, and J. Carreira, “Perceiver: General perception with iterative attention,” in *Proceedings of the 38th International Conference on Machine Learning*, ser. Proceedings of Machine Learning Research, M. Meila and T. Zhang, Eds., vol. 139. PMLR, 18–24 Jul 2021, pp. 4651–4664.

[41] T. Wang, A. Roberts, D. Hesslow, T. L. Scao, H. W. Chung, I. Beltagy, J. Launay, and C. Raffel, “What language model architecture and pretraining objective work best for zero-shot generalization?” in *Proceedings of the 39th International Conference on Machine Learning (ICML)*, vol. 162. PMLR, 2022, pp. 23,671–23,694.

[42] T. Lin, Y. Wang, X. Liu, and X. Qiu, “A survey of transformers,” *AI Open*, vol. 3, pp. 111–132, 2022.

[43] A. Kramberger, E. Shahriari, A. Gams, B. Nemec, A. Ude, and S. Hadadin, “Passivity based iterative learning of admittance-coupled dynamic movement primitives for interaction with changing environments,” in *2018 IEEE/RSJ International Conference on Intelligent Robots and Systems (IROS)*, 2018, pp. 6023–6028.

[44] N. Hogan, “Impedance control: An approach to manipulation — part i: Theory,” *Journal of Dynamic Systems, Measurement, and Control*, vol. 107, no. 1, pp. 1–7, 1985.

[45] ———, “A general actuator model based on nonlinear equivalent networks,” in *2014 IEEE International Conference on Robotics and Automation (ICRA)*. IEEE, 2014, pp. 2647–2653.

[46] ———, “Impedance and interaction control,” in *2015 IEEE-RAS 15th International Conference on Humanoid Robots (Humanoids)*. IEEE, 2015, pp. 1–7.

[47] J. Lachner, “A geometric approach to robotic manipulation in physical human-robot interaction,” Ph.D. dissertation, University of Twente, 2022.

[48] J. Lachner, F. Allmendinger, E. Hobert, N. Hogan, and S. Stramigoli, “Energy budgets for coordinate invariant robot control in physical human-robot interaction,” *The International Journal of Robotics Research*, vol. 40, no. 8–9, pp. 968–985, 2021.

[49] S. Schaal, “Is imitation learning the route to humanoid robots?” *Trends in cognitive sciences*, vol. 3, no. 6, pp. 233–242, 1999.

[50] A. J. Ijspeert, J. Nakanishi, H. Hoffmann, P. Pastor, and S. Schaal, “Dynamical movement primitives: learning attractor models for motor behaviors,” *Neural computation*, vol. 25, no. 2, pp. 328–373, 2013.

[51] M. C. Nah, J. Lachner, and N. Hogan, “Robot control based on motor primitives: A comparison of two approaches,” *The International Journal of Robotics Research*, vol. 43, no. 12, pp. 1959–1991, 2024.

[52] M. C. Nah, J. Lachner, F. Tessari, and N. Hogan, “On the modularity of elementary dynamic actions,” in *2024 IEEE/RSJ International Conference on Intelligent Robots and Systems (IROS)*. IEEE, 2024, pp. 1398–1405.

[53] C. Chi, Z. Xu, S. Feng, E. Cousineau, Y. Du, B. Burchfiel, R. Tedrake, and S. Song, “Diffusion policy: Visuomotor policy learning via action diffusion,” *The International Journal of Robotics Research*, 2024.

[54] K. Shoemake, “Animating rotation with quaternion curves,” *SIGGRAPH Comput. Graph.*, vol. 19, no. 3, p. 245–254, Jul. 1985.

[55] C. M. Bishop, “Training with noise is equivalent to tikhonov regularization,” *Neural Computation*, vol. 7, no. 1, pp. 108–116, 01 1995.

[56] J. Lachner, F. Tessari, A. M. W. Jr., M. C. Nah, and N. Hogan, “Divide et impera: Decoding impedance strategies for robotic peg-in-hole assembly,” *arXiv preprint arXiv:2410.01054*, 2025.

[57] J. Carvalho, A. T. Le, M. Baierl, D. Koert, and J. Peters, “Motion planning diffusion: Learning and planning of robot motions with diffusion models,” in *2023 IEEE/RSJ International Conference on Intelligent Robots and Systems (IROS)*, 2023, pp. 1916–1923.

[58] J. Lachner, M. C. Nah, S. Stramigoli, and N. Hogan, “Exp [licit] an educational robot modeling software based on exponential maps,” in *2024 IEEE International Conference on Advanced Intelligent Mechatronics (AIM)*. IEEE, 2024, pp. 1359–1366.

[59] D. E. Whitney, “Quasi-Static Assembly of Compliantly Supported Rigid Parts,” *Journal of Dynamic Systems, Measurement, and Control*, vol. 104, no. 1, pp. 65–77, 03 1982. [Online]. Available: <https://doi.org/10.1115/1.3149634>

[60] S. Hirai and K. Tanie, “Remote center compliance with adaptive compliance control,” in *Proceedings of the IEEE International Conference on Robotics and Automation*. IEEE, 1990, pp. 468–473.

[61] J. Lachner, F. Allmendinger, S. Stramigoli, and N. Hogan, “Shaping impedances to comply with constrained task dynamics,” *IEEE Transactions on Robotics*, vol. 38, no. 5, pp. 2750–2767, 2022.

[62] A. Albu-Schaffer, C. Ott, U. Frese, and G. Hirzinger, “Cartesian impedance control of redundant robots: recent results with the DLR-light-weight-arms,” *IEEE International Conference on Robotics and Automation*, pp. 3704–3709, 2003.

APPENDIX A

ENERGY-BASED IMPEDANCE CONTROLLER

A. Elastic Force

The translational restoring force arises $\mathbf{f} \in \mathbb{R}^3$ from the displacement between the end-effector position $\mathbf{p} \in \mathbb{R}^3$ and the reference ZFT position $\mathbf{p}_0 \in \mathbb{R}^3$. It is modeled as

$$\mathbf{f} = \mathbf{K}_t (\mathbf{p}_0 - \mathbf{p}) - \mathbf{B}_t \dot{\mathbf{p}}, \quad (29)$$

where $\mathbf{K}_t \in \mathbb{R}^{3 \times 3}$ is the translational stiffness matrix, $\mathbf{B}_t \in \mathbb{R}^{3 \times 3}$ the damping matrix, and $\dot{\mathbf{p}} \in \mathbb{R}^3$ the end-effector translational velocity.

For implementation, the damping is expressed proportional to stiffness as

$$\mathbf{B}_t = \lambda_t \mathbf{K}_t, \quad (30)$$

with λ_t the translational positive time constant.

B. Elastic Moment

Rotational restoring moments $\mathbf{m} \in \mathbb{R}^3$ are expressed relative to the ZFT orientation $\mathbf{q}_0 \in SU(2)$, represented in axis-angle form as (\mathbf{u}_0, θ_0) . The elastic moment is given by

$$\mathbf{m} = \mathbf{K}_r \theta_0 \mathbf{u}_0 - \mathbf{B}_r \boldsymbol{\omega}, \quad (31)$$

where $\mathbf{K}_r \in \mathbb{R}^{3 \times 3}$ is the rotational stiffness matrix, $\mathbf{B}_r \in \mathbb{R}^{3 \times 3}$ the rotational damping matrix, and $\boldsymbol{\omega} \in \mathbb{R}^3$ the angular velocity of the end-effector.

Analogous to translations, the damping term is chosen proportional to stiffness:

$$\mathbf{B}_r = \lambda_r \mathbf{K}_r, \quad (32)$$

with λ_r the rotational positive time constant.

C. Damping design

The damping design was formulated to ensure that energy dissipation scales consistently with both the commanded stiffness $\mathbf{K} \in \mathbb{R}^{3 \times 3}$ and the task-space inertia $\mathbf{\Lambda} \in \mathbb{R}^{3 \times 3}$. This construction was applied in the translational and rotational subspaces alike. To account for numerical issues near singular configurations, $\mathbf{\Lambda}$ was computed using a damped least-squares method.

A user-selected positive time constant $d > 0$ defines the diagonal damping ratio matrix

$$\mathbf{D} = d \mathbf{I}_3. \quad (33)$$

The symmetric positive semidefinite square roots $\sqrt{\mathbf{\Lambda}}$ and $\sqrt{\mathbf{K}}$ are obtained by eigendecomposition for $\mathbf{\Lambda}$ and elementwise for \mathbf{K} . As presented in [62], an intermediate damping matrix is constructed as

$$\mathbf{b} = \sqrt{\mathbf{\Lambda}} \mathbf{D} \sqrt{\mathbf{K}} + \sqrt{\mathbf{K}} \mathbf{D} \sqrt{\mathbf{\Lambda}}. \quad (34)$$

From \mathbf{b} , a scalar damping coefficient is computed to normalize the dissipation relative to the overall stiffness:

$$\lambda = \frac{2 \operatorname{tr}(\mathbf{b})}{\operatorname{tr}(\mathbf{K})} = \frac{2 \operatorname{tr}(\mathbf{b})}{k_x + k_y + k_z}. \quad (35)$$

The final damping matrix can then be expressed as

$$\mathbf{B} = \lambda \mathbf{K}. \quad (36)$$

APPENDIX B

ZFT-BASED TELEMANIPULATION WITH APPLE VISION PRO

To enable spatially unconstrained teleoperation, we employed the VisionProTeleop framework (Figure 10) [27]. The Apple Vision Pro continuously captured the operator’s hand motion in six degrees of freedom without requiring markers or external infrastructure. This setup provided full spatial flexibility, allowing the robot to be teleoperated even in occluded or confined environments.

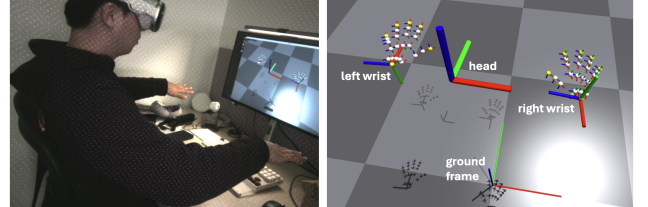


Fig. 10: Pose tracking and visualization with Apple Vision Pro. Left: operator performing telemanipulation. Right: virtual reconstruction of wrist, hand, and head poses in a 3D scene. [27]

Within the VisionProTeleop framework, the operator’s hand pose was continuously tracked and expressed as a homogeneous transformation matrix.

The hand was modeled as a 27-joint kinematic skeleton, including wrist, base, intermediate, and fingertip joints. In our implementation, the handMiddleFingerKnuckle (index 11) was selected as the primary keypoint for translation and rotation.

Pose data were transferred via shared memory between the Python-based VisionProTeleop module and the C++ robot controller. In this way, the Apple Vision Pro provided a seamless method to generate sZFT ground truth data through markerless and physically unconstrained teleoperation. The implementation of the teleoperation interface is available in our GitHub repository¹¹.

APPENDIX C

PEG-IN-HOLE EXPERIMENTS

This appendix complements the main results by reporting stiffness adaptation for the circular and square pegs. The corresponding results for the star peg are already presented in the main text (Fig. 9). The experimental setup, controllers, and parameters matched the main text: baseline stiffness $K_{t,i,\max} = 800 \text{ N/m}$ and $K_{r,i,\max} = 150 \text{ Nm/rad}$, damping as in Appendix A-C, and force/moment thresholds of 1 N and 1 Nm. All quantities are expressed in the robot base frame. The lower plots in both of the following figures show the relative translational and rotational factors $\rho_{t,i}$ and $\rho_{r,i}$ from (27), which modulate the reduction terms in the adaptive law.

For the circular peg, rotational symmetry about the end-effector z -axis makes the final yaw alignment irrelevant. Stiffness modulation is therefore dominated by translational factors, with only minor rotational adjustments. For the square

¹¹<https://github.com/StrokeAIRobotics/DiffusionBasedImpedanceLearning>

peg, alignment with the edges increased sensitivity to off-axis contact. This yielded stronger directional reductions in both translation and rotation when axes contributed little to the sZFT, while stiffness remained high along task-relevant directions.

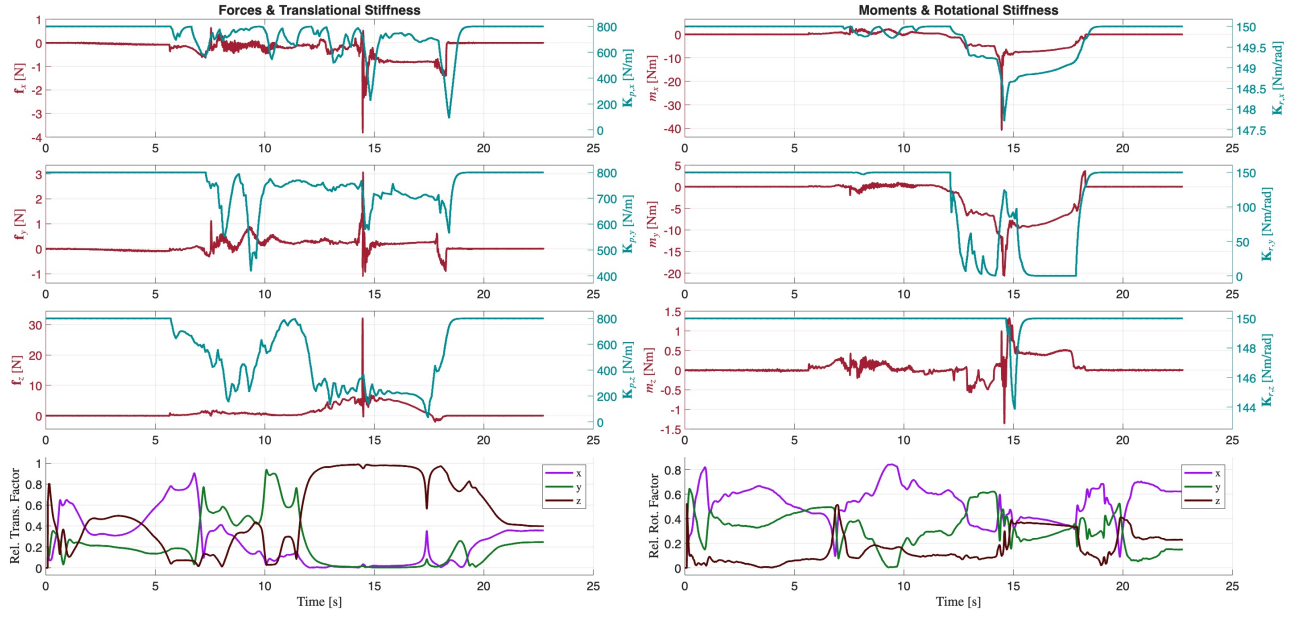


Fig. 11: Insertion of a circular peg. Measured external wrenches and commanded translational and rotational stiffness during insertion. The lower plots show the relative translational and rotational factors (Eq. (27)) and their influence on stiffness modulation. Rotational adjustments are small due to axial symmetry; stiffness reductions occur primarily along directions with low task relevance.

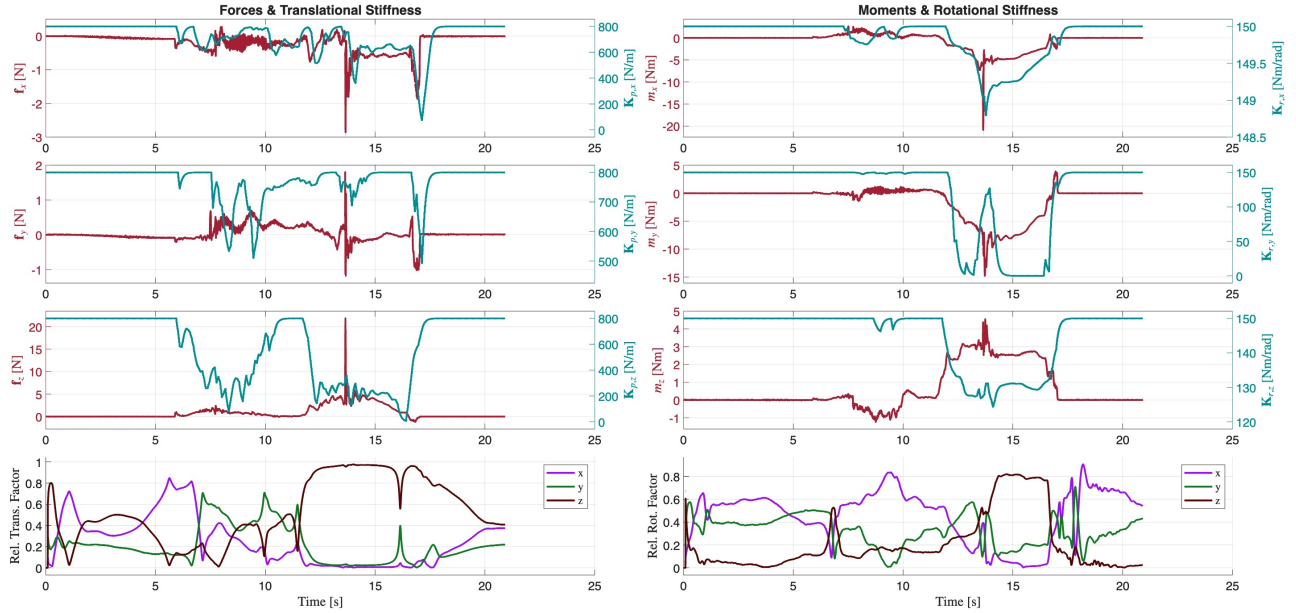


Fig. 12: Insertion of a square peg. Measured external wrenches and commanded translational and rotational stiffness during insertion. The lower plots show the relative translational and rotational factors (Eq. (27)). Directional reductions are more pronounced than for the circular peg, reflecting the need to relieve off-axis contact while preserving stiffness along the insertion and alignment axes.